Strain localization and the onset of dynamic weakening in fault gouge

S.A.F. Smith[1], S. Nielsen[2] & G. Di Toro[3,4]

[1]Department of Geology, University of Otago, Dunedin 9054, New Zealand

[2]Rock Mechanics Laboratory, Department of Earth Sciences, Durham University, Durham, England

[3]Istituto Nazionale di Geofisica e Vulcanologia (INGV), Rome 00143, Italy

[4]Dipartimento di Geoscienze, Università degli Studi di Padova, Via G. Gradenigo 6, 35131, Padova, Italy

Corresponding author e-mail: steven.smith@otago.ac.nz

Corresponding author telephone: +64 03 479 7515

Corresponding author fax: +64 03 479 7527

Abstract

To determine the role of strain localization during dynamic weakening of gouge at seismic slip rates, single-slide and slide-hold-slide experiments were conducted on 2-3-mm thick layers of calcite gouge at normal stresses up to 26 MPa and slip rates up to 1 m s^{-1}. Microstructures were analyzed from short displacement (<0.35 m) experiments stopped prior to and during the transition to dynamic weakening. In fresh calcite gouge layers, dynamic weakening occurs after a prolonged initial strengthening phase that becomes shorter with increasing normal stress and decreasing layer thickness. Strain is initially distributed across the full thickness of the gouge layer, but quickly becomes localized to a boundary-parallel, high-strain shear band c. 20 μm wide. During the initial strengthening phase the shear band broadens to become c. 100 μm wide at peak stress. The transition to dynamic weakening in calcite gouges is associated with a change from layer dilation to compaction and the appearance of many short and isolated slip surfaces within the shear band. Each individual slip surface is surrounded by aggregates of extremely fine grained and tightly packed calcite, interpreted to result from grain welding driven by local frictional heating in the shear band. By the end of dynamic weakening, deformation is extremely well localized to a single 2-3-μm wide principal slip surface, flanked by layers of recrystallized gouge. Calcite gouge layers re-sheared following a hold period behave mechanically like solid cylinders of calcite marble, due to reactivation of the principal slip surface formed during the first slide reducing the effective gouge layer thickness to a few microns. Our results suggest that formation of a high-strain shear band is a critical precursor to dynamic weakening in calcite gouges. Microstructures are most compatible with dynamic weakening in gouges resulting from a thermally triggered mechanism such as flash heating that requires both a high degree of strain localization and a minimum slip velocity to activate.

Keywords: Localization; Gouge; Dynamic Weakening; Microstructure; Earthquakes

Highlights:

- Experiments on calcite gouges to investigate strain localization and dynamic weakening
- Formation of high-strain shear band is critical precursor to dynamic weakening
- Dynamic weakening correlates with formation of short slip surfaces in shear band
- Observations compatible with gouge dynamic weakening by flash heating in shear band
- Re-sheared calcite gouge layers behave like solid marble

1. Introduction

Mid- to upper-crustal crustal fault zones contain layers of finely comminuted material known as fault gouge, formed by particle fracturing, surface wear and fluid-rock interactions (e.g. Ben-Zion and Sammis, 2003; Chester and Logan, 1987; Engelder, 1974; Scholz, 1987; Sibson, 1977). Field observations indicate that fault displacements are often focused in to narrow gouge-bearing fault cores (e.g. Ben-Zion and Sammis, 2003; Caine et al., 1996; Chester and Chester, 1998; Chester et al., 2004; Faulkner et al., 2010; Sagy and Brodsky, 2009; Schulz and Evans, 2000; Wibberley and Shimamoto, 2003). There is also increasing evidence to suggest that seismic slip during earthquakes occurs largely within gouge-bearing slip zones on the order of a few millimeters or less in thickness (e.g. Boullier et al., 2009; Chester and Chester, 1998; Collettini et al., 2013; De Paola et al., 2008; Fondriest et al., 2012; Heesakkers et al., 2011; Li et al., 2012; Mizoguchi et al., 2008; Otsuki et al., 2003; Sibson, 2003; Smith et al., 2011; Wibberley and Shimamoto, 2003).

Laboratory experiments have demonstrated that bare rock surfaces and gouge layers experience dynamic weakening when the slip velocity and sliding displacement approach values characteristic of earthquakes (Di Toro et al., 2011). A variety of physical mechanisms have been proposed to explain the dynamic weakening behavior observed in the laboratory and postulated to occur in natural faults. In particular, mechanical and microstructural data collected from experiments performed on solid rocks (bare surfaces) are consistent with the activity of flash heating and weakening at asperity contacts (Beeler et al., 2008; Goldsby and Tullis, 2011; Kohli et al., 2011; Rice, 2006), silica gel lubrication (Di Toro et al., 2004) and frictional melting (Di Toro et al., 2006; Nielsen et al., 2008).

Gouge layers deformed at high velocities typically show a narrow (<100 μm) and fine-grained shear localization zone cut by a discrete sliding surface or multiple surfaces coated with extremely small ("nano") or sintered grains (e.g. Brantut et al., 2011; De Paola et al., 2011; Ferri et al., 2011;

66 Fondriest et al., 2013; Han et al., 2010a; Han et al., 2011; Kitajima et al., 2010; Smith et al., 2013;
67 Tisato et al., 2012; Yao et al., 2013a). The onset of dynamic weakening in experiments performed with
68 blocks of granite (Reches and Lockner, 2010) was attributed to wear of the solid rock material,
69 formation of a gouge layer, and the development of a thin actively deforming zone (the "third body" of
70 Reches and Lockner, 2010) that was suggested to lubricate the sliding surface. In the short-
71 displacement experiments of Goldsby and Tullis (2011) and Kohli et al. (2011) the evolution of shear
72 stress during slip acceleration and deceleration prompted the authors to suggest that flash heating and
73 weakening occurred following strain localization in a thin gouge layer formed by wear between solid
74 rock cylinders. More recently, Proctor et al. (2014) compared the frictional behavior of serpentinite
75 gouges and solid rings (bare surfaces) of serpentinite. They found that higher slip velocities were
76 required to initiate dynamic weakening in the gouges compared to the solid samples, and concluded
77 that flash weakening in the gouges was delayed due to initially distributed deformation.

78 In general, the above experimental studies have shown that the presence of gouges is likely to be an
79 important factor in the dynamic evolution of fault strength during seismic slip. This is in addition to the
80 critical role played by gouges in determining the stability of faults during the nucleation phase of
81 earthquakes (e.g. Beeler et al., 1996; Giger et al., 2008; Ikari et al., 2011; Logan et al., 1979; Mair and
82 Marone, 1999; Marone, 1998; Marone et al., 1990; Niemeijer et al., 2008; Rathbun and Marone, 2010;
83 Scholz, 2002; Scruggs and Tullis, 1998; Scuderi et al., 2013). However, most previous experimental
84 studies performed at high-velocities have focused on gouge microstructure at the end of relatively
85 large-displacement experiments, and thus the correlation between microstructure (e.g. strain
86 localization) and mechanical behavior remains poorly understood.

87 The objective of the present paper is to report on an experimental and microstructural investigation
88 of strain localization and its influence on dynamic weakening in granular calcite gouges. Calcite is an

important, and in some cases dominant, mineral in many seismically active regions worldwide, where main shocks and aftershocks nucleate within and propagate through thick sequences of carbonates (Italy, e.g. 2009 Mw 6.3 L'Aquila earthquake, Chiarabba et al., 2009; Chiaraluce, 2012; Greece, e.g. 1995 Ms 6.6 Western Macedonia earthquake, Jackson, 1994; Himalayan orogenic belt, e.g. 2008 Mw 7.9 Wenchuan earthquake, Verberne et al., 2010). We employed a rotary-shear friction apparatus to deform layers of calcite gouge at high slip velocities and moderately high normal stresses. By tightly controlling the total experimental displacements, we systematically investigated the relationships between gouge mechanical behavior and microstructural evolution prior to and during the transition to dynamic weakening.

2. Methods

2.1 Sample preparation and starting materials

Experiments were performed with SHIVA (**S**low- to **Hi**gh-**V**elocity rotary-shear friction **A**pparatus; Fig 1a) at the INGV, Rome (Di Toro et al., 2010; Niemeijer et al., 2011) using a sample holder for incohesive materials (gouge) with rotary and stationary parts (Figures 1b,c). The rotary side of the gouge holder consists of a base plate (*a* in Figure 1b) and inner and outer rings (*g, i* in Figure 1b) that prevent gouge extrusion during the experiments. The inner and outer rings slide over a base disc (*h* in Figure 1a) located in the stationary base plate (*f* in Figure 1b). Both the rotary base plate and the stationary base disc have a crosshatch pattern of surface roughness where in contact with the gouge layer (Figure 1c; amplitude of surface roughness 400 μm, wavelength 800 μm). Axial load on the gouge layer is applied directly through the stationary base plate by the loading column of SHIVA (Di Toro et al., 2010). Axial load on the inner and outer sliding rings is modulated by five outer springs (*j* in Figures 1a,b) and one inner spring (*e* in Figure 1a). Calibration tests (Smith et al., 2013) indicate that the contribution to measured torque values from the sliding rings is negligible (<2.5% of measured

torque) at the normal stresses used in these experiments (generally >8.5 MPa, two experiments at 4 MPa).

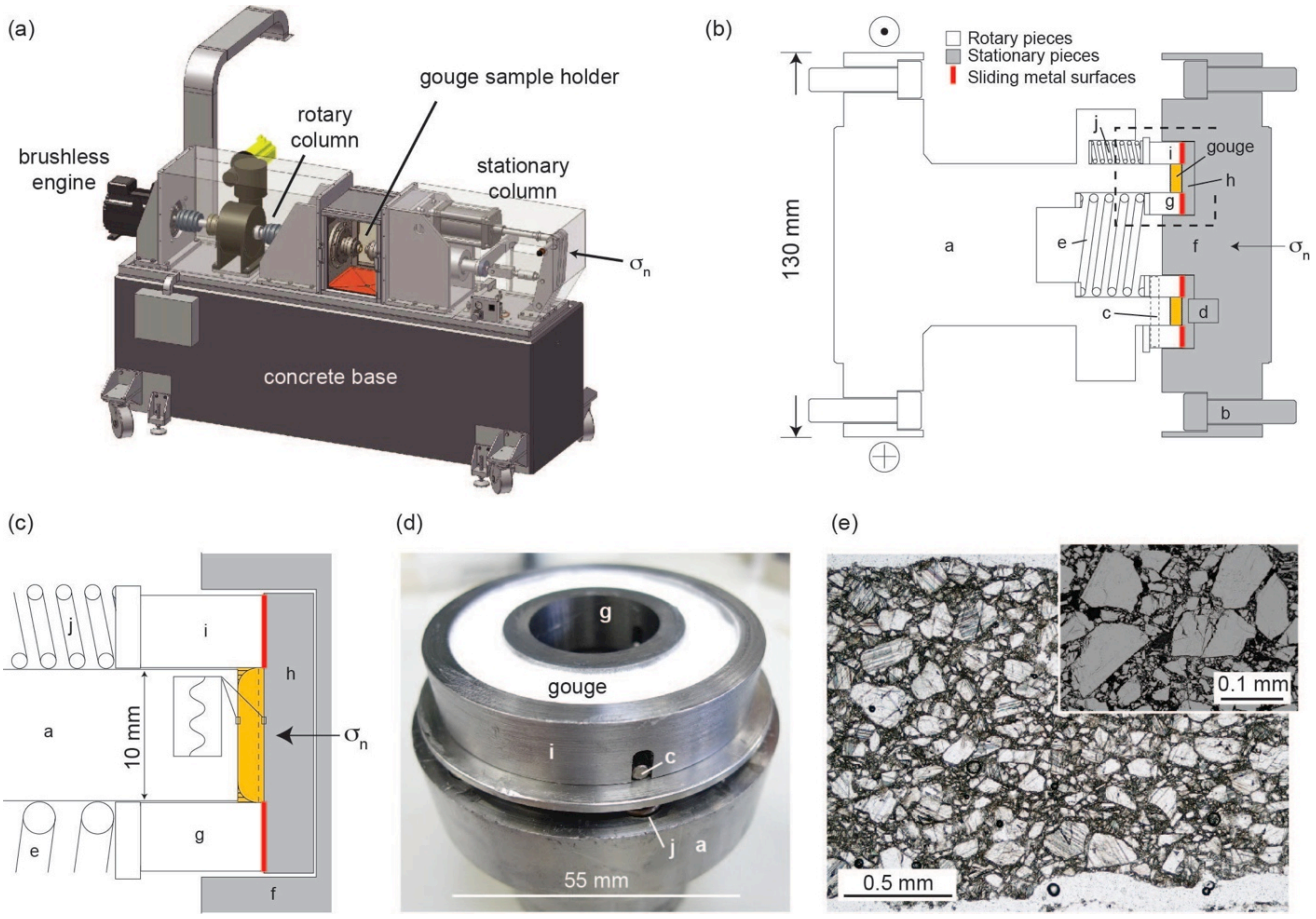

Figure 1: Experimental set-up and sample assembly for gouge experiments. **(a)** Photograph of the SHIVA apparatus with main components labeled as followed: - (b) Schematic diagram of gouge holder. Details of calibration tests can be found in the Supplementary Information of Smith et al. (2013). Labeled pieces of the gouge holder are: a, rotary base plate; b, mounting bolts; c, rotary driving pins; d, anti-rotation pins for base disc; e, inner spring; f, stationary base plate; g, inner sliding ring; h, stationary base disc; i, outer sliding ring; j, outer springs. The gouge layer is contained between the outer and inner rings that slide over the base disc (sliding contacts in red). Normal stress (σ_n) is applied to the gouge layer by the loading assembly behind the stationary column (Di Toro et al., 2010). Normal stress on the sliding rings is modulated by inner and outer springs. **(c)** Enlargement of part b showing

124 the gouge compartment of the sample holder [modified after Proctor et al., 2014]. The dashed line
125 indicates the region where localization typically occurs in the gouge layers. The hatched areas in the
126 corners of the gouge layer remain relatively undeformed due to the sample geometry (similar to the
127 shielding effects discussed in (Beeler et al., 1996)). Where in contact with the gouge layer, the rotary
128 and stationary pieced have a cross-hatched pattern of surface roughness with wavelength 800 μm and
129 amplitude 400 μm. (d) Photograph of calcite gouge layer (35/55 mm int./ext. diameters) prior to an
130 experiment. Labeled pieces are defined in part a. A thin layer of high-temperature grease is applied to
131 the sliding surfaces of the rings to reduce friction. **(e)** Optical photomicrograph in plane polarized light
132 (main image) and backscattered scanning electron microscope detail of calcite gouge compacted to 15
133 MPa. The starting material has a grain size <250 μm. During initial compaction, some fracturing and
134 twinning of calcite grains occurs.

135

136 The gouge starting material was prepared by grinding fragments of Carrara marble in a pestle
137 and mortar. The gouge was passed through a 250-μm sieve and all particles that passed through the
138 sieve were included in the starting gouge. Powder X-ray diffraction analysis together with Scanning
139 Electron Microscope (SEM) observations indicate that the starting material is composed of >99 wt%
140 calcite, with <1 wt% dolomite, quartz, and muscovite as accessory phases (typical minor phases in
141 Carrara marble: Smith et al., 2013). Each experiment used 5 g or 3 g of calcite gouge, resulting in ring-
142 shaped gouge layers (35/55 mm int./ext. diameters; Figures 1b-d) with initial thicknesses of,
143 respectively, c. 3 mm and c. 2 mm (Figures 1b-d).

144 **2.2 Experimental and analytical procedures**

145 All of the experiments were performed under room-dry conditions (room humidity varied
146 between 50% and 80%). Each experiment consisted of the following steps: 1) preparation of the gouge

147 layer following the procedures outlined in Section 2a; 2) mounting of the gouge sample holder in
148 SHIVA and loading of the gouge layer to the target normal stress; 3) deformation of the gouge layer
149 under the desired conditions of maximum slip velocity, acceleration and deceleration rate, and total
150 displacement; and, 4) unloading and recovery of the deformed gouge layer for microstructural analysis.
151 Experiments were performed at constant normal stresses of 4 – 26 MPa and maximum slip velocities
152 up to 3.4 m s^{-1}. Total displacement in each experiment was controlled precisely using two digital
153 encoders located on the rotary column. One encoder with an angular resolution of x μm was used to
154 control and measure displacements up to 0.01 m. The second encoder with a lower angular resolution
155 of x μm was used to control and measure displacements greater than 0.01 m. Axial displacements were
156 measured using a Linear Variable Differential Transformer (LVDT). Experimental data (e.g. axial load,
157 torque, axial displacements, angular rotation) were acquired at a frequency up to 25 kHz, and
158 determination of total displacement, slip rate, and shear stress followed methods outlined in Di Toro et
159 al. (2010).

160 Two types of experiment were performed on calcite gouges: single-slide experiments and slide-
161 hold-slide experiments. In single-slide experiments, only one slip pulse was imposed on the gouge
162 layer before it was recovered for microstructural analysis. In slide-hold-slide experiments, two slip
163 pulses were imposed under identical conditions, separated by a hold period lasting x-x seconds during
164 which the normal stress was held constant and no angular movements of the rotary column were
165 detected.

166 Following most of the experiments, the deformed gouge layers were cohesive and flinty, and
167 could be recovered quite easily for microstructural analysis. Fragments of the gouge layers were
168 impregnated under vacuum using low-viscosity epoxy, and petrographic sections cut perpendicular to
169 the gouge layers and approximately parallel to the slip direction were prepared for microstructural

observations using a transmitted-light petrographic microscope and a Zeiss Sigma VP Field-Emission Scanning Electron Microscope (SEM; in the Otago Centre for Electron Microscopy, University of Otago) operating in backscattered mode (acquisition conditions: accelerating voltage 15 kV, working distance 6-8.5 mm). Energy-dispersive X-ray Spectroscopy (EDS) on the SEM was used to produce the element distribution map in Figure 6b.

2.3 Experiments with solid cylinders (bare surfaces) of marble

To compare the mechanical behavior of calcite gouges to solid rocks (i.e. bare surfaces) of the same mineralogical composition, single-slide experiments were performed on hollow cylindrical samples (30/50 mm int./ext. diameter) of Carrara marble. Each experiment used newly prepared cylindrical samples. The bare sliding surfaces were ground with 320 grit sandpaper before each experiment. The experimental procedures for the Carrara marble cylinders were the same as those detailed above, except that a different sample holder was used to grip the solid cylinders (sample procedures for solid cylinders described in Di Toro et al., 2010; Niemeijer et al., 2011; Violay et al., 2013).

3. Results

3.1 Dynamic weakening in calcite gouges and bare surfaces

Figure 2a shows the evolution of shear stress and slip velocity for two representative slide-hold-slide experiments performed at 8.5 MPa normal stress on (i) a 2 mm-thick layer of calcite gouge (red data, s753) and (ii) bare surfaces of calcite marble (grey data, s758). Slip is reported on a log scale to highlight the mechanical behavior in the early stages of slip. For clarity, only the slip velocity data for the gouge experiment are shown, but the slip velocity evolution was nearly identical in both experiments. Each slide had 2 m of displacement, a maximum slip velocity of 2.25 m s^{-1}, and

acceleration and deceleration rates of 7 m s^2. The slides were separated by a static hold period of 40 seconds. Figure 2b shows variations in axial displacement during the two experiments, where positive changes indicate axial shortening and negative changes indicate dilation.

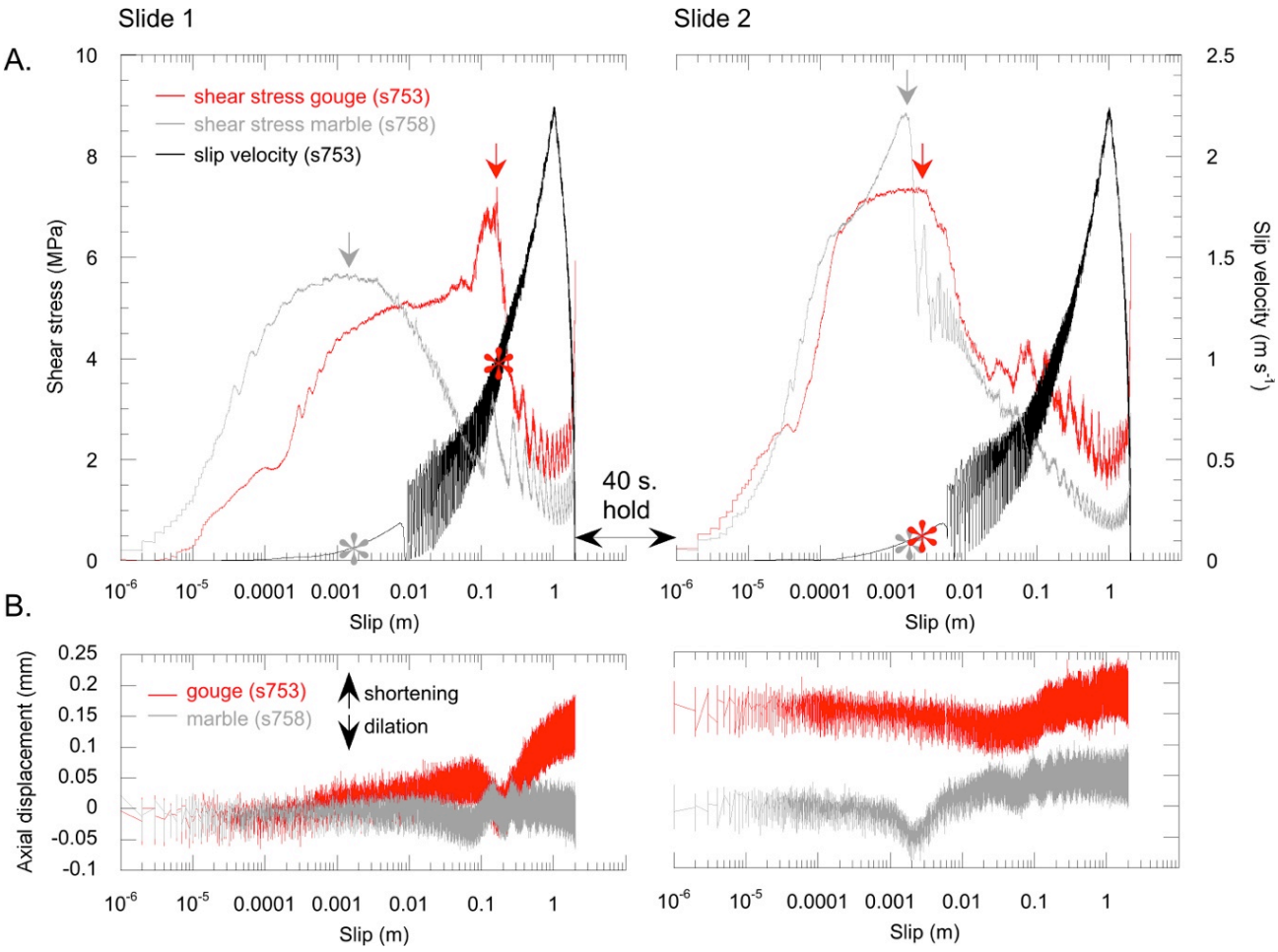

Figure 2: Evolution of shear stress, slip velocity and axial shortening during slide-hold-slide experiments on calcite gouge (s753) and bare surfaces of calcite marble (s758). Experiments were performed under identical conditions (8.5 MPa normal stress; 2.25 m s^{-1} maximum slip velocity; acceleration and deceleration of 7 m s^2; 2 m displacement during each slide; slides separated by a static hold period of 40 seconds). On the curves of shear stress and axial displacement, the systematic oscillations in the data (spaced every c. 0.125 m in the marble experiments and c. 0.15 m in the gouge experiments) are due to small misalignments between the solid marble cylinders or small variations in

gouge layer thickness. **(a)** Slide 1: the onset of weakening in calcite marble (grey arrow) occurred after c. 0.002 m of slip at a slip velocity of c. 0.1 m s^{-1} (grey star on slip velocity curve). Instead, the calcite gouges showed a prolonged phase of strengthening prior to peak shear stress and dynamically weakened (red arrow) after ~0.2 m of slip at a much higher slip velocity of ~1 m s^{-1} (red star on slip velocity curve). Slide 2: the onset of weakening in both calcite marble and calcite gouge occurred after ~0.002 m of slip at a slip velocity of ~0.1 m s^{-1}. **(b)** During slide 1, axial shortening was negligible in the calcite marble, but a significant phase of dilation occurred in the calcite gouge layer prior to peak stress (between 0.1 – 0.2 m slip). Dilation ended in the gouge layer at peak stress and was followed by compaction of ~150 μm. During slide 2, ~50 μm of further compaction took place in the calcite gouge layer after ~0.05 m of slip. In the calcite marble, a short phase of dilation lasting ~1 mm was recorded just prior to peak stress (between 0.001 – 0.002 m).

These two experiments illustrate significant differences in the mechanical behavior of calcite gouge layers and bare surfaces at seismic slip rates. During slide 1, the calcite marble initially strengthened reaching peak shear stress (5.5 MPa) after c. 0.002 m of slip (approximated by grey arrow in Figure 2a). The marble then dynamically weakened to a much lower shear stress of 1 MPa after c. 1 m of slip. Dynamic weakening in the marble initiated at a slip velocity of c. 0.1 m s^{-1} (see grey star on slip velocity curve in Figure 2a).

No significant axial displacements were recorded during slide 1 with the marble cylinders (Fig 2b). The oscillations observed in the axial displacement data (and the corresponding shear stress data) for the marbles are systematically spaced every c. 0.125 m, which corresponds to the average circumference of the solid marble cylinders. The oscillations in these data are thought to reflect a small

misalignment between the rotary and stationary columns of the deformation apparatus, or slightly non-parallel sliding surfaces of the marble samples.

In comparison to the marble, the calcite gouge showed a prolonged phase of strengthening at the start of slide 1 (Figure 2a). Dynamic weakening in the gouge initiated after c. 0.2 m of slip (approximated by red arrow in Figure 2a) at a slip velocity of c. 1 m s^{-1} (see red star on slip velocity curve in Figure 2a). The minimum shear stress obtained by the gouge layer following dynamic weakening was slightly higher than in the solid marble samples (Figure 2a). The gouge layer initially shortened by ~50 μm, then between 0.08 – 0.2 m a transient phase of dilation was recorded (~100 μm dilation; Figure 2b). Dilation ended once peak shear stress was reached in the gouge layer, upon which renewed shortening occurred. Overall shortening of c. 150 μm was recorded in the gouge layer during slide 1 (Figure 2b).

During slide 2, the evolution of shear stress was similar in both the calcite marble and calcite gouge (Figure 2a). In both experiments, dynamic weakening initiated after c. 0.002 m of slip (grey and red arrows in Figure 2a) at a slip velocity of c. 0.1 m s^{-1} (grey and red stars on slip velocity curve in Figure 2a). The decay from peak to minimum shear stress occurred over roughly the same slip distance in both experiments, although as observed in slide 1 the minimum shear stress obtained by the gouge layer was slightly higher than the solid marble cylinders (Figure 2a).

Axial displacements during slide 2 in the gouges were relatively minor compared to slide 1, although ~50 μm of additional shortening took place after c. 0.03 m of slip (Figure 2b). At the start of the additional shortening during slide 2, there was a slight increase in shear stress, possibly reflecting minor gouge extrusion between the sliding rings. In the marble, a short-lived phase of dilation occurred between c. 0.001-0.002 m, just prior to peak shear stress (Figure 2b). Following peak shear stress, shortening of ~100 μm was observed.

248 Figure 3 summarizes the slip distance required to initiate dynamic weakening in calcite gouge
249 layers (e.g. grey and red arrows in Figure 2.) and its dependence on normal stress and gouge layer
250 thickness for 31 single-slide and slide-hold-slide experiments with an acceleration rate of 7 m s^2. Also
251 shown are data from 13 single-slide experiments on solid cylinders (bare surfaces) of calcite marble.
252 The main results can be summarized as follows (Figure 3):

253 i) During slide 1 in calcite gouges (red and green filled symbols) the initial strengthening phase
254 lasts between c. 3-30 cm. The length of the strengthening phase decreases with increasing normal stress
255 between 4 – 26 MPa, and it also decreases for thinner gouge layers. Above a normal stress of 15-20
256 MPa, the length of the strengthening phase may remain constant with increasing normal stress,
257 although more data are required to confirm this.

258 ii) During slide 2 in gouges (red and green open symbols), the strengthening phase is much
259 shorter, lasting on the order a few millimeters or less. The strengthening phase in slide 2 is independent
260 of both normal stress and layer thickness.

261 iii) The length of the strengthening phase during slide 2 in gouges is comparable to that
262 observed in solid cylinders of calcite marble (grey symbols) over the range of investigated normal
263 stresses.

264

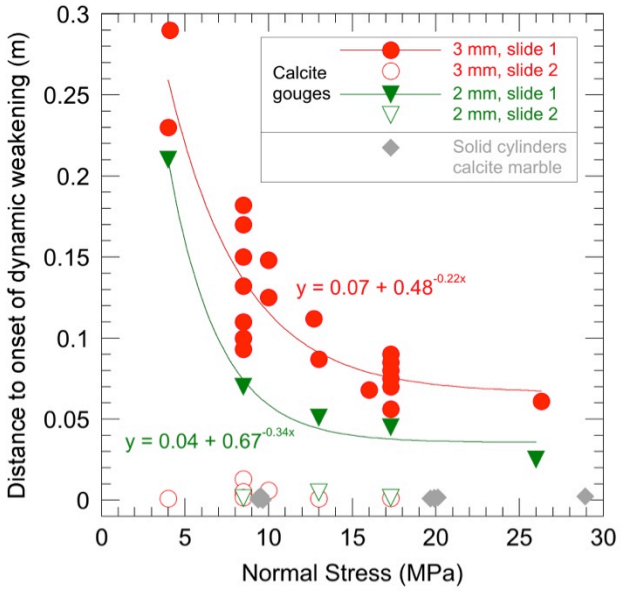

Figure 3: Distance to onset of dynamic weakening vs. normal stress for 31 single-slide and slide-hold-slide experiments performed on 2- or 3-mm thick layers of calcite gouge, as well as 13 single-slide experiments on solid cylinders (bare surfaces) of calcite marble. In all experiments the acceleration and deceleration rates were 7 m s^2. The data for slide 1 in gouges are approximated using best-fit exponential decay functions (R^2 = 0.81 for 3 mm thick layers, R^2 = 0.99 for 2 mm thick layers).

3.2 Velocity dependence and hysteresis

In experiments on calcite gouge, a marked hysteresis effect was observed in plots of shear stress versus slip velocity. Figure 4 shows shear stress versus slip velocity for a representative slide-hold-slide experiment (s363) performed on a 3 mm-thick layer of calcite gouge (σ_n = 8.5 MPa, maximum slip velocity 1 m s^{-1}, each slide 2 m of displacement). As slip velocity increased at the start of slide 1 (red data), shear stress initially increased rapidly, followed by a prolonged phase of more gradual strengthening up to a slip velocity of c. 0.8 m s^{-1} (Figure 4). At c. 0.8 m s^{-1} rapid dynamic weakening occurred, with shear stress decreasing to much lower values as the maximum slip velocity (c. 1 m s^{-1})

was approached (Figure 4). During deceleration, shear stress increased roughly linearly with decreasing velocity and ultimately recovered to around 90% of its peak value. The rate at which shear stress recovered during deceleration was lower than the rate at which dynamic weakening proceeded, resulting in an overall clockwise path in shear-stress-velocity space (Figure 4).

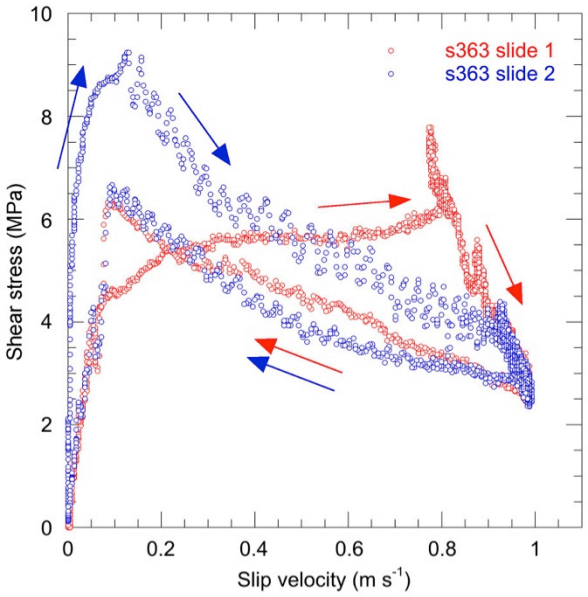

Figure 4: Hysteresis in shear stress data observed in a representative slide-hold-slide experiment (s363; 3 mm-thick calcite gouge layer, 8.5 MPa normal stress, 1 m s^{-1} maximum slip velocity, acceleration and deceleration 7 m s^{2}). The arrows indicate the sequence of data acquisition during acceleration and deceleration. During slide 1 (red data), dynamic weakening initiated at a relatively high slip velocity of ~0.8 m s^{-1}. During deceleration, shear stress increased again, but at a rate much lower than during dynamic weakening. During slide 2 (blue data), weakening initiated at a slip velocity almost an order of magnitude lower than slide 1 (~0.1 m s^{-1}), and the evolution of shear stress during acceleration and deceleration was similar (i.e. the hysteresis effect was much less pronounced than in slide 1).

During slide 2 (following a hold period of 42.6 seconds), the calcite gouge again strengthened rapidly as the slip velocity increased from zero, but dynamic weakening initiated at a much lower slip velocity of c. 0.1-0.15 m s^{-1} (Figure 4). Above this slip velocity, shear stress decreased to a minimum value comparable to that obtained in slide 1. During deceleration of slide 2, the shear stress recovered to around 70% of its peak value and followed a nearly identical path to slide 1 (Figure 4). Overall, the marked hysteresis that characterized the shear stress-velocity evolution of slide 1 was much less pronounced during slide 2.

3.3 Microstructural evolution of calcite gouge layers

A series of experiments was performed at 8.5 MPa normal stress with increasing total displacements in the range of 0.01-0.35 m to provide insights in to the microstructural evolution of the calcite gouge layers during the transition from strengthening to dynamic weakening. Observations from three of these experiments are summarized below (Figures 5,7,8). All three experiments were performed with 3 mm-thick gouge layers, imposing a target acceleration rate of 6 m s^2 and a target maximum slip velocity of 1.1 m s^{-1}. An additional small displacement (0.028 m) experiment was performed at a higher normal stress of 17.3 MPa in which a dolomite strain marker was constructed in the calcite gouge layer prior to shearing (Figure 6).

3.3.1 0.01 m slip (s784)

Due to the small displacement in this experiment the maximum slip velocity obtained was 0.27 m s^{-1} (Figure 5a). The total displacement was approximately an order of magnitude lower than the c. 0.1 m required for dynamic weakening under these experimental conditions (see experiment s493, grey curve, in Figure 5a and data in Figure 3 at 8.5 MPa). Axial shortening of c. 50 μm was measured after 0.01 m of slip (Figure 5a).

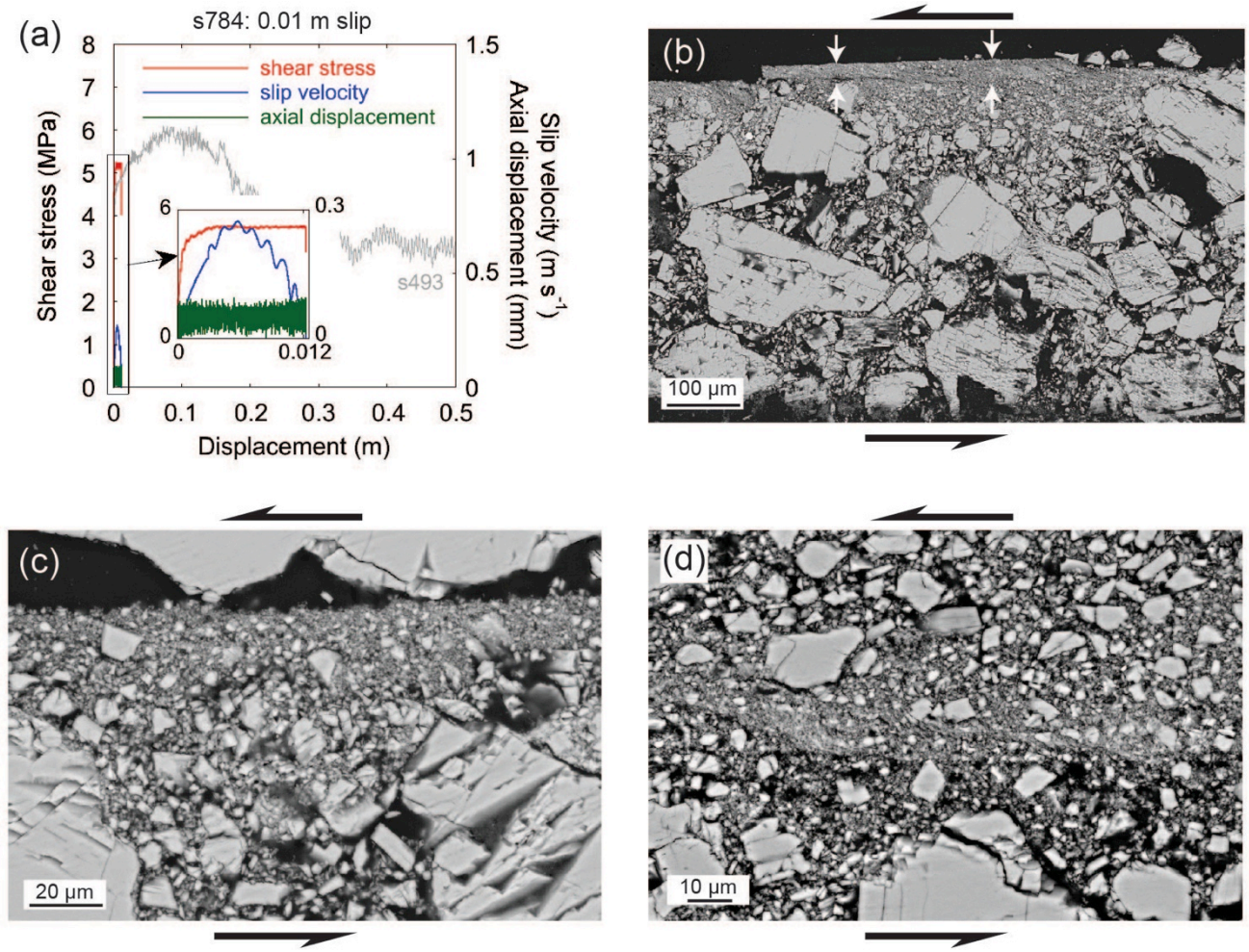

317

318 **Figure 5:** Mechanical data and microstructures of experiment s784, stopped after 0.01 m of slip. (a)
319 Plot of shear stress, slip velocity and axial displacement vs. slip. The inset box shows a detail of the
320 first 0.01 m of slip. The grey curve (also in Figures 7, 9, 10) shows the shear stress evolution of
321 experiment s493, performed under identical conditions but taken to a total displacement of 1 m. (b)
322 SEM image of gouge layer. A narrow shear band of fine grain size (outlined by the white arrows) is
323 developed close to the stationary side of the gouge holder (see approximate position in Figure 1c). The
324 bulk of the gouge layer is much coarser grained and resembles the starting material. (c) Detail of fine-
325 grained shear band showing angular calcite clasts < 10 µm in size embedded within a much finer-
326 grained calcite matrix. The shear band is < 20 µm thick. Larger clasts outside the shear band are

heavily fractured along cleavage planes. (d) Some parts of the shear band contain domains of particularly fine grain size, appearing as lighter patches on SEM images. The example shown here is c. 10 μm wide and 100 μm long and runs sub-horizontally across the middle of the image.

The calcite gouge layer contains a well-defined shear band up to 20 μm thick (between white arrows in Figure 5b), defined in SEM images by a much finer grain size and more compact appearance compared to the surrounding gouge layer (Figures 5b,c). The grain sizes and overall appearance of the bulk of the gouge layer (i.e. outside the slip zone) are similar to the gouge starting material (compare Figures 1e and 5b). As observed in all gouge experiments that reached slip velocities >0.1 m s^{-1}, the shear band developed sub-parallel to gouge layer boundaries (i.e. a Y-shear (Logan et al., 1979)) and at a distance of c. 100 μm from the surface roughness on the stationary side of the gouge holder (see position of dashed line in Figure 1c). The shear band consists of angular to sub-angular calcite grains < 10 μm in size that are surrounded by a finer-grained calcite matrix (Figure 5c). Internally, the shear band contains elongate domains (up to 100 μm long and 10 μm wide) of extremely fine grain size aligned sub-parallel to the shear band boundaries (Figure 5d).

3.3.2. Strain distribution before the transition to dynamic weakening

Experiment s781 was performed at a higher normal stress of 17.3 MPa (Figure 6) and stopped after 0.028 m of slip. At this normal stress the onset of dynamic weakening in calcite gouge occurs after 0.05 – 0.1 m of slip (see example of s626, grey curve, in Figure 6a and data in Figure 3). The maximum slip velocity reached in s781 was 0.4 m s^{-1} and overall c. 50 μm of axial shortening was measured (Figure 6a).

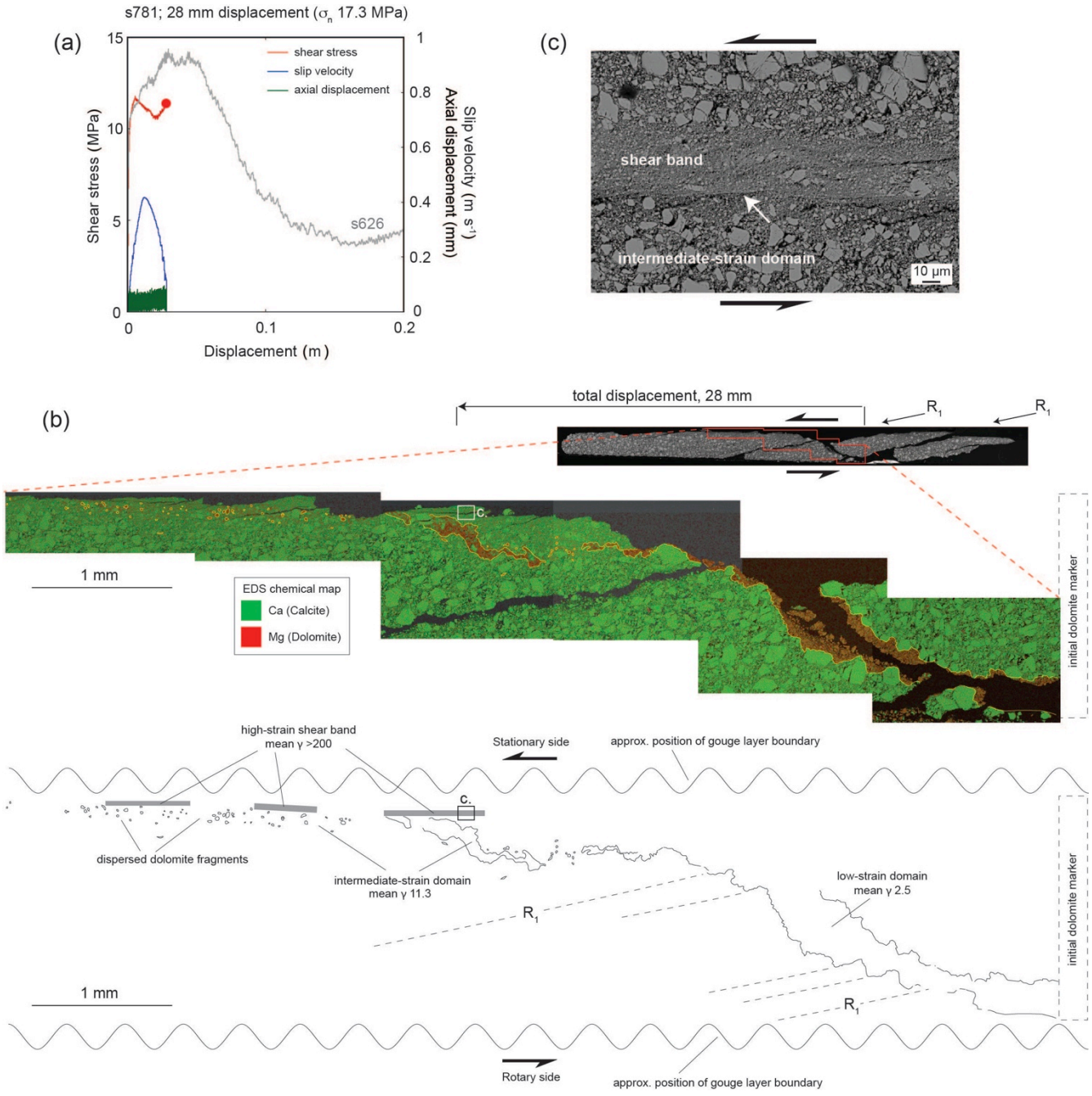

Figure 6: Experiment s781 (17.3 MPa normal stress) performed with a dolomite strain marker and stopped after 0.028 m of slip. **(a)** Evolution of shear stress, slip velocity and axial displacement in experiment s781. Also shown is the shear stress evolution in experiment s626 (grey curve) performed under identical conditions. Experiment s626 indicates that the onset of dynamic weakening under these conditions occurs after ~0.05 m of slip (also see data in Figure 3). **(b)** SEM-EDS images of the calcite

355 gouge layer and dolomite strain marker. The greyscale image shows an SEM mosaic of the entire
356 gouge layer and a representation of the total experimental displacement. The colored image shows an
357 EDS chemical map of Mg (dolomite) and Ca (calcite) distribution in the gouge layer that was used to
358 reconstruct the strain distribution after shearing. The dolomite marker was initially sub-perpendicular
359 to gouge layer boundaries. The lower line drawing shows a tracing of the dolomite strain marker and an
360 interpretation of the three strain domains distinguished from the geometry of the marker. A series of
361 R_1-Riedel shears offset the edges of the strain marker in the low-strain domain. **(c)** SEM image
362 (location shown in part b) of the high-strain shear band. The shear band is 50-100 μm wide and much
363 finer grained than the adjacent gouge. The white arrow shows where one edge of the shear band is
364 defined by a discrete surface.

365

366 Prior to the experiment, a c. 300 μm-wide "wall" of relatively fine-grained (particle size
367 fraction <63 μm) dolomite gouge was constructed approximately perpendicular to the slip direction and
368 gouge layer boundaries to act as a strain marker (Figure 6b). Dolomite is distinguished in the EDS
369 chemical map shown in Figure 6b by a red color (corresponding to Mg) and calcite by a green color
370 (corresponding to Ca). The geometry of the dolomite strain marker reveals a number of significant
371 microstructures within the gouge layer and it can also be used to broadly define three strain "domains".
372 From the rotary to the stationary side the three domains are (Figure 6b):

373 (1) A low-strain domain c. 1.5 mm thick that accommodated c. 3.8 mm of slip. The mean shear strain
374 (γ) in this domain (calculated as slip/thickness) is c. 2.5. The grain sizes in this domain are comparable
375 to the gouge starting material (e.g. Figure 1e). The edges of the strain marker are intact and roughly
376 parallel, and there is little or no mixing between the dolomite marker and the surrounding calcite
377 gouge. However, the edges of the marker are offset by a number of R_1-Riedel shears defined by bands

of grain size reduction and open fractures (the latter assumed to have formed by normal stress unloading). The Riedel shears lie at angles of 15-20° to the gouge layer boundaries and have measured synthetic (i.e. the same as the bulk shear sense) offsets of 100-200 μm.

(2) An intermediate-strain domain c. 0.4 mm thick that accommodated c. 4.5 mm of slip. In this domain mean γ is 11.3, the dolomite strain marker is heavily disrupted, and there is some mixing between the dolomite and calcite gouges. In the region closest to the high-strain shear band (see below) the dolomite marker becomes increasingly disrupted to form a layer containing only dispersed dolomite fragments.

(3) A high-strain shear band between 50 - 100 μm thick that accommodated up to 19.7 mm of slip (total experimental slip of 28 mm minus the slip in the low- and intermediate-strain domains), resulting in mean $\gamma > 200$. SEM analysis indicates that both boundaries of the high-strain shear band are defined by an abrupt reduction in grain size and, in places, more discrete surfaces (Figure 6c). It is not possible to estimate how much displacement occurred in the sliver of calcite gouge lying between the shear band and the stationary side of the gouge holder, and hence the estimate of 19.7 mm displacement for the shear band is a maximum estimate. However, given the relatively coarse grain size preserved in the sliver (Figure 6c; comparable to the intermediate-strain domain) the displacement is considered to be minor. Within the high-strain shear band, the dolomite strain marker is completely disaggregated, although in the slip direction small grains of dolomite derived from the strain marker can be found dispersed throughout. Internally, the shear band contains diffuse layering defined mainly by pockets of slightly coarser-grained gouge (Figure 6c). Within and surrounding the shear band, calcite grains are cut by intergranular fractures (Figure 6c).

3.4.3. 0.2 m slip (s631)

Experiment s631 was stopped after 0.2 m of slip (Figure 7a). During deceleration the shear stress recovered to nearly its peak value. Comparison to other experiments performed under the same conditions (e.g. s493, grey curve, in Figure 7a; data in Figure 3) indicates that s631 was stopped approximately mid-way through the dynamic weakening phase. A total of c. 200 μm of axial shortening was recorded, although this included a transient phase of dilation between c. 0.05-0.12 m (Figure 7a). Dilation ended once peak shear stress was reached and dynamic weakening initiated.

Compared to experiments stopped before the onset of dynamic weakening (e.g. Figures 5,6), the bulk of the gouge layer has a much finer grain size (Figure 7b), indicating that some distributed deformation and grain size reduction occurred even after the high-strain shear band had formed. The shear band in this experiment is up to 100 μm wide (between white arrows in Figure 7b), similar to that observed at an earlier stage in the strain history (i.e. s781 in Figure 6). The shear band contains sub-angular to sub-rounded calcite grains <10 μm in size (Figure 7c). The most significant difference in the microstructure of the shear band compared to pre-peak stress is that it contains many short (<100 μm) isolated slip surfaces that are sub-parallel to the shear band boundaries (Figure 7c). SEM observations show that thin (<10 μm) and elongate (<100 μm) regions of extremely fine-grained (<1 μm) and tightly packed calcite aggregates surround each slip surfaces (Figures 7c,d). Within these regions individual grains or grain boundaries cannot be recognized (Figure 7e). The fine-grained regions are commonly cut by small brittle fractures oriented at high angles to the shear band boundaries and showing micron-scale offsets (white arrows in Figure 7c). These fractures are assumed to have formed late in the experiments (during deceleration) or during sample preservation, suggesting that the short slip surfaces and surrounding fine-grained regions are more cohesive than the shear band matrix.

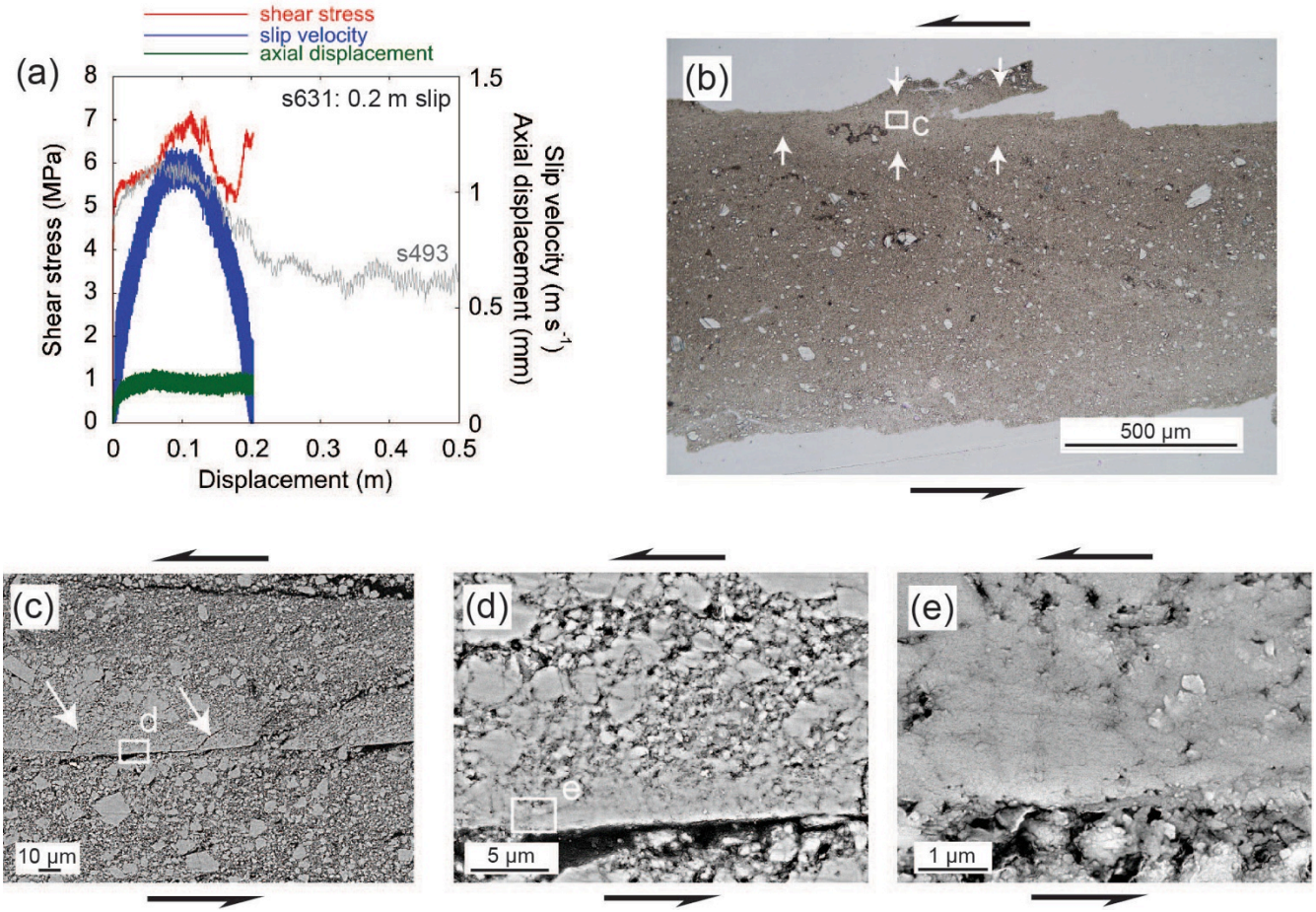

Figure 7: Mechanical data and microstructures of experiment s631, stopped after 0.2 m of slip. (a) Plot of shear stress, slip velocity and axial displacement. Comparison with s493 indicates that the experiment was stopped approximately mid-way through the dynamic weakening phase. Transient dilation of the gouge layer occurred during the strengthening phase, and ended once peak shear stress was reached. (b) Optical photomicrograph in plane-polarized light showing the fine-grain size of the bulk gouge layer and the c. 100-µm wide shear band (between white arrows). (c) SEM image of the shear band showing two discrete slip surfaces associated with regions of extremely fine grain size and low porosity. Small cracks with micron-scale offsets are indicated by white arrows. (d) Detail of one of the slip surfaces in part c. The slip surface is flanked by regions up to 10 µm wide in which the grain size is < 1 µm and the porosity is low compared to the surrounding shear band matrix. (e) Detail of d at

high magnification showing the extremely fine-grained and tightly-packed nature of the calcite aggregates. Individual grains or grain boundaries cannot be recognized.

3.4.4. 0.35 m slip (s492)

Experiment s492 was stopped after 0.35 m of slip, at the end of the dynamic weakening phase (i.e. as the shear stress reached "steady state" values; Figure 8a). A transient phase of dilation was recorded during the strengthening phase, which ended once peak shear stress was reached.

After 0.35 m of slip, the fine-grained shear band that formed at shorter displacements is cut by a single, continuous and relatively planar slip surface (delineated by white arrows in Figures 8b,c) along which the gouge layer parted during sample recovery. When removed from the sample holder, the slip surface was extremely cohesive, had flinty fracture, and reflected natural light in a specular way. In the petrographic microscope, the slip surface appears as a discrete fracture <2-3 μm wide cutting the surrounding fine-grained shear band (Figure 8c). Adjacent to the slip surface is a layer c. 10 μm thick that has a uniform color when observed with the sensitive-tint (gypsum) plate inserted in the petrographic microscope, suggesting that it has a crystallographic-preferred orientation (CPO; Figure 8c inset). There are also small, tabular fragments with a CPO in the surrounding shear band (e.g. yellow arrow in Figure 8c inset), interpreted as pieces of cohesive slip surface material that were broken off and reworked during slip. SEM observations of the material coating the 2-3 μm-wide slip surface show aggregates of highly elongate grains with irregular, rounded to lobate grain boundaries (Figure 8d). The grains are a few tens to a few hundreds of nanometers long and consistently aligned in the direction of shear, forming a well-defined shape-preferred orientation at an angle of c. 20° to the slip surface (measured clockwise in Figure 8d). The shear band material with a CPO adjacent to the slip surface is formed of calcite grains up to 1 μm in size with well defined, straight to slightly curved grain

boundaries and roughly polygonal grain shapes (Figure 8e). Boundaries between adjacent grains commonly meet at triple junctions with interfacial angles of c. 120° (Figure 8e). As the slip surface is approached, the grains in this layer become smaller (<500 nm close to the slip surface) and develop more elongate grain shapes (Figure 8e). The grains closest to the slip surface are aligned in the shear direction and possess a shape-preferred orientation at an angle of c. 20° to the slip surface (Figure 8e).

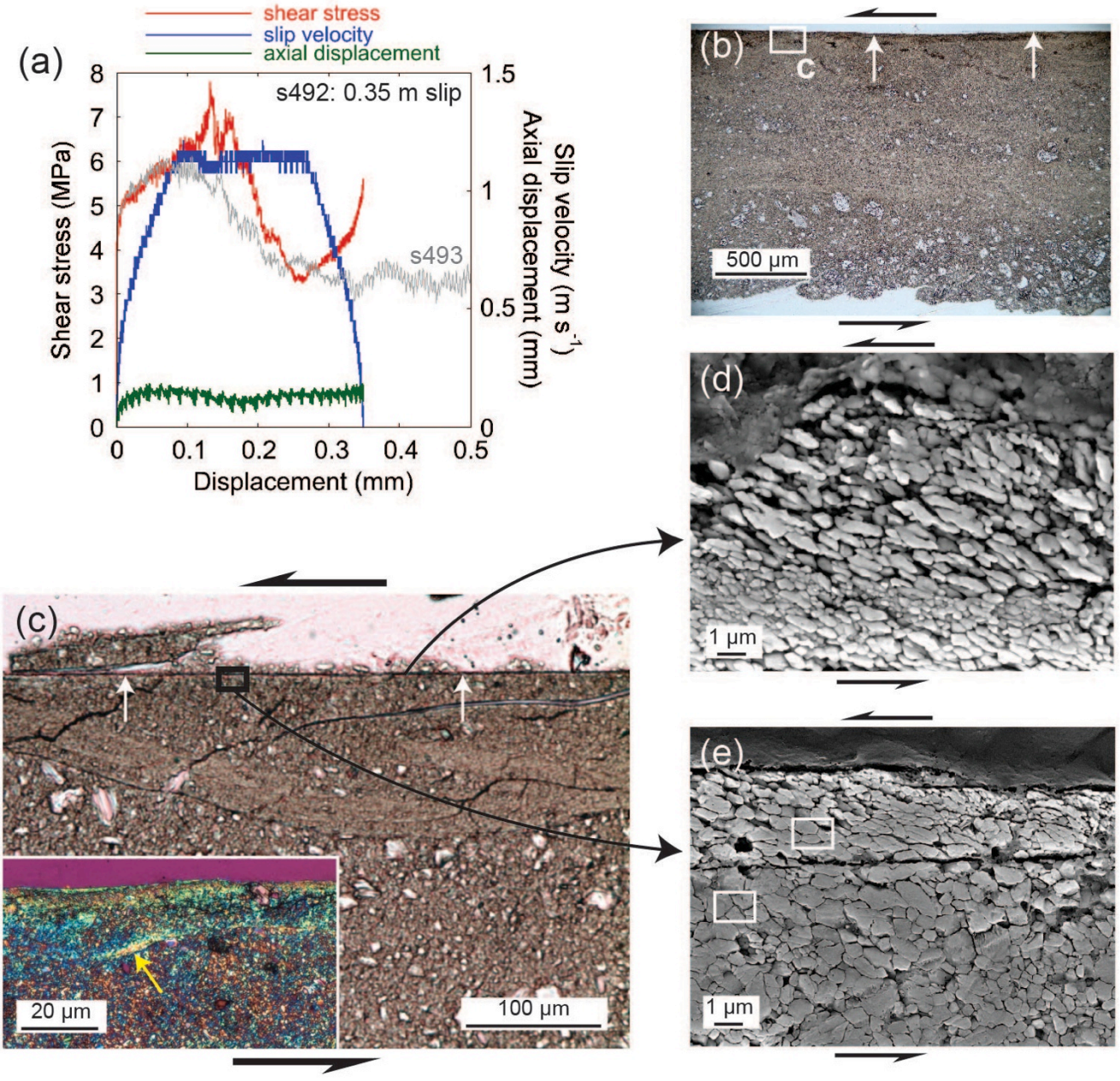

Figure 8: Mechanical data and microstructures of experiment s492, stopped after 0.35 m of slip. (a) Plot of shear stress, slip velocity and axial displacement. This experiment was stopped at the end of the dynamic weakening phase. (b) Optical photomicrograph in plane polarized light showing a single, discrete slip surface (marked by white arrow). (c) Detail of part b showing the discrete, 2-3-μm wide slip surface (white arrows) surrounded by the extremely fine-grained shear band. The inset shows an image of the slip surface and adjacent shear band with the sensitive-tint (gypsum) plate inserted in to the petrographic microscope. The uniform yellow and blue colors in a layer c. 10 μm thick immediately adjacent to the slip surface indicate the presence of a crystallographic-preferred orientation (CPO). Small tabular fragments with a CPO (yellow arrow) are also found in the shear band, probably representing pieces of cohesive slip surface material broken off and reworked during shear. (d) SEM image of the material coating the 2-3-μm wide slip surface. The elongate grains coating the slip surface are on the order of tens to hundreds of nanometers in size. (e) SEM image of the shear band layer containing a CPO. In this layer, calcite grains are micron-sized and have straight to slightly curved grain boundaries that often meet at grain triple-junctions (two examples in white boxes).

4. Discussion

4.1 Strain localization and dynamic weakening in calcite gouges

Both calcite gouges and solid cylinders (bare surfaces) of calcite marble experience dynamic weakening at moderate normal stresses (4 – 26 MPa) and slip velocities between ~0.1 – 1 m s^{-1}. However, much higher displacements and slip velocities are required to initiate dynamic weakening in the gouge layers. At the highest normal stresses investigated here (26 MPa), the displacement and slip velocity at the onset of dynamic weakening in 2-3 mm thick calcite gouge layers are approximately an

order of magnitude higher than for solid cylinders (bare surfaces) of calcite marble or calcite gouge layers re-sheared following a static hold period.

Microstructural observations of experiments stopped at different displacements indicate that during shearing at high velocity, strain is initially distributed across the full thickness of the gouge layer. Localization to a boundary-parallel, high-strain shear band occurs in <0.01 m of slip, even although dynamic weakening does not occur until higher displacements (e.g. 0.1-0.2 m at 8.5 MPa normal stress; Figure 3). The shear band is initially quite thin (<20 μm) but broadens with displacement during the strengthening phase until it is c. 100 μm thick around peak stress (similar to the observations in Yao et al., 2013a). Once formed, the shear band accommodates a majority of subsequent slip, although some distributed deformation must occur outside the shear band to explain the progressive grain size reduction observed in the bulk of the gouge layer. Prior to peak shear stress, the shear band is active at the same time as sets of R_1 - Riedel shears (stage 1, Figure 9). Given the prevalence of angular to sub-angular calcite grains within the shear band, and the occurrence of intergranular fracturing in the bulk of the gouge layer, cataclasis is likely to be the most important deformation process prior to peak shear stress.

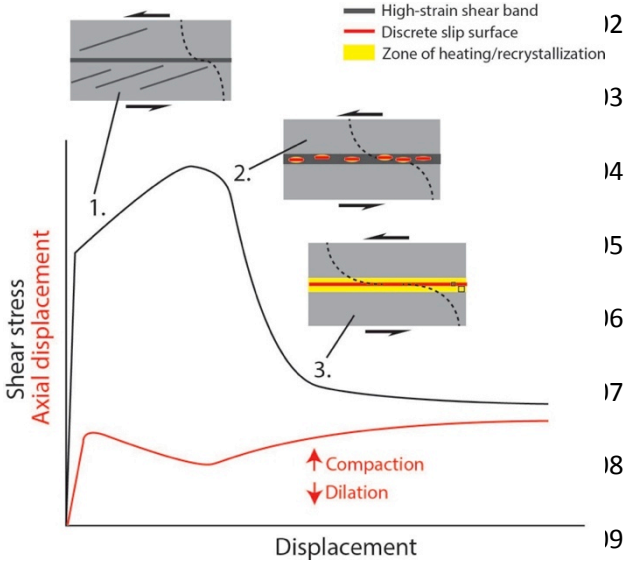

Figure 9: Schematic illustration of the mechanical and microstructural evolution of calcite gouge layers sheared at high velocity. 1: pre-peak stress, 2: peak stress, 3: end of dynamic weakening. Dashed lines approximate strain distribution.

510 The transition to dynamic weakening in calcite gouges is associated with a switch from layer
511 dilation to compaction and the appearance of short and discontinuous slip surfaces within the
512 boundary-parallel shear band (stage 2, Figure 9), each of which is surrounded by a region containing
513 extremely fine-grained and tightly packed calcite aggregates. We interpret the slip surfaces and
514 surrounding aggregates to represent zones of gouge in which the local slip velocities during shearing
515 were high enough to allow frictional heating and welding of the extremely fine calcite grains. Welding
516 is suggested on the basis that i) the aggregates around the slip surfaces have much lower porosity than
517 the surrounding shear band matrix, ii) individual grains and grain boundaries cannot be recognized in
518 the aggregates even at high magnifications, suggesting coalescence of sub-micron particles, and iii) the
519 aggregates are cohesive enough to fracture, suggesting that individual particles are strongly bound to
520 one another. In experiments performed under similar conditions to those applied here, Mitchell et al.
521 (2014) detected CO_2 degassing from mixed calcite-dolomite gouge layers after less than 8 mm of
522 displacement, before peak stress was reached. This indicates that temperatures in the gouge layers can
523 locally reach the decomposition temperatures of carbonates (around 550°C for dolomite and 700°C for
524 calcite; e.g. De Paola et al., 2011; Rodriguez-Navarro et al., 2009; Samtani et al., 2002) during the
525 initial increments of shearing (Han et al., 2007). Given that carbonate decomposition temperatures are
526 significantly higher than the c.180°C required for crystal-plastic deformation of calcite (e.g. Burkhard,
527 1990), the experimental results of Mitchell et al. (2014) support the assertion that welding of extremely
528 fine-grained calcite aggregates could occur locally in the high-strain shear band after displacements
529 corresponding to peak stress. Sawai et al. (2012) and Togo and Shimamoto (2012) interpreted grain
530 welding to have occurred in high-velocity (<1.3 m s^{-1}) and large-displacement (up to 48 m)
531 experiments on clay- and quartz-rich gouges on the basis of surface area measurements. In their
532 experiments, gouge surface area decreased with increasing amounts of slip (and power density),
533 suggesting particle aggregation during shearing. Accompanying microstructural analysis indicated that

534 aggregation was probably due to welding of grain boundaries driven by the frictional heat produced in
535 localized slip zones (Sawai et al., 2012; Togo and Shimamoto, 2012). Similar conclusions regarding
536 grain welding as an active deformation process in high-velocity gouge experiments were recently
537 published in Yao et al. (2013a,b).

538 By the end of dynamic weakening, deformation is fully localized, with the formation of a single
539 2-3-μm wide slip surface cutting the shear band (stage 3, Figure 9). The slip surface itself is coated
540 with ultra-fine grains and is flanked by layers of calcite (Figures 8, 9) that have many of the
541 microstructural characteristics (e.g. CPO and SPO; straight to slightly curved grain boundaries; grain-
542 boundary triple junctions) of plastically-deformed and recrystallized calcite mylonites (e.g. Barnhoorn
543 et al., 2004; Bestmann et al., 2000; Bestmann and Prior, 2003; Ebert et al., 2007; Herwegh and Kunze,
544 2002; Trullenque et al., 2006). Similar fabrics observed in high-velocity gouge experiments with total
545 displacements >1 m have been attributed to recrystallization and grain growth caused by bulk frictional
546 heating along the localized slip surface (Brantut et al., 2011; Fondriest et al., 2013; Han et al., 2010b;
547 Kim et al., 2010; Ree et al., 2014; Smith et al., 2013; Yao et al., 2013b).

548 The microstructural evolution that we have documented in calcite gouges indicates that strain
549 localization to a thin shear band is a critical precursor to dynamic weakening. Our observations are
550 most compatible with dynamic weakening in calcite gouges resulting from a thermally triggered
551 mechanism such as flash heating that requires both a high degree of strain localization and a minimum
552 slip velocity (c. 0.1 m s^{-1}) to activate (Beeler et al., 2008; Goldsby and Tullis, 2011; Proctor et al.,
553 2014; Rice, 2006).

554 **4.2 Hysteresis in shear stress – velocity data**

555 In the short-displacement experiments of Goldsby and Tullis (2011) and Kohli et al. (2011),
556 performed on a range of solid rocks (granite, quartzite, novaculite, albite, gabbro, serpentine), the

557 authors observed a hysteresis effect in shear stress-velocity data during acceleration and deceleration,
558 similar to that observed in the present calcite gouge experiments (Figure 4). They concluded that during
559 the initial stages of high-velocity sliding (and/or during the slow-velocity run-in phase in the case of
560 Kohli et al. (2011)), a thin gouge layer (<40 μm) was quickly formed by wear of the solid rock
561 surfaces. Because of this, up to several millimeters of slip were required to localize deformation within
562 the gouge layer to such a degree that efficient heating could take place at grain contacts, leading to
563 flash weakening (Goldsby and Tullis, 2011; Kohli et al., 2011). A marked hysteresis effect during high-
564 velocity shearing of quartz-rich gouge layers at 0.56 MPa normal stress has also been noted previously
565 by Sone and Shimamoto (2009).

566 Our experimental and microstructural observations, following those of Goldsby and Tullis
567 (2011) and Kohli et al. (2011), suggest that the hysteresis observed in the calcite gouge data reflects
568 progressive strain localization during acceleration to high velocity. In the slide-hold-slide experiments
569 reported here, the hysteresis during the first slide is more pronounced than in the experiments of
570 Goldsby and Tullis (2011) and Kohli et al. (2011) because of the relatively thick starting gouge layers
571 (2-3 mm in these experiments as opposed to wear of bare rock surfaces producing gouge layers less
572 than tens of microns thick in the case of Goldsby and Tullis (2011) and Kohli et al. (2011)). However,
573 during the second slide the calcite gouge layers show much faster dynamic weakening, similar to solid
574 cylinders of calcite marble. Based on microstructural observations, a possible explanation for this
575 mechanical behavior is that deformation during the second slide is quickly localized to the discrete slip
576 surface that forms by the end of dynamic weakening in slide 1 (e.g. stage 3 in Figure 9). Reactivation
577 of the discrete slip surface during the second slide would reduce the effective gouge layer thickness to a
578 few microns at most, explaining why the re-sheared gouge layers behave in a similar manner to solid
579 cylinders of calcite marble. This mechanism is supported by SEM observations that show the
580 microstructure of gouges deformed in slide-hold-slide experiments is essentially identical to that at the

end of the dynamic weakening phase in single-slide experiments (e.g. stage 3 in Figure 9), the only notable difference being a thicker zone of gouge recrystallization adjacent to the slip surface. Further to this, multiple slip surfaces and reworked fragments of slip surface were not identified in the microstructure of slide-hold-slide experiments, suggesting that distributed deformation did not occur in the gouge layers at the start of slide 2.

4.3 Implications

In natural fault zones, the mechanical properties of fresh gouge layers (i.e corresponding to slide 1 in our experiments) are likely to be most relevant during seismic slip because of dynamic formation of gouge ahead of the rupture tip. Reches and Dewers (2005) showed that a mode II rupture propagating at 98% of the Rayleigh speed will result in tensile stresses of up to 3 GPa and volumetric strain rates exceeding 10^5 s^{-1} in the few millimeters around the rupture tip. Due to such intense stress (and temperature) pulses the fault rocks surrounding the rupture tip are expected to pulverize (Reches and Dewers, 2005; Sammis and Ben-Zion, 2008). Observations made in underground mines closely following small (<M2.2) shallow-focus earthquakes support the idea that layers of fine-grained gouge ("rock flour") can be dynamically generated (e.g. Heesakkers et al., 2011; Stewart et al., 2001). Additionally, the interaction of fault surface asperities during seismic slip will result in the formation of fresh gouge (Candela et al., 2009; Griffith et al., 2010; Power et al., 1987; Power et al., 1988; Sagy and Brodsky, 2009; Sagy et al., 2007). This means that even in granular fault rocks that have been recrystallized or cemented during the interseismic period (e.g. Bruhn et al., 1994; Gratier and Gueydan, 2007; Sibson, 1987; Tenthorey and Cox, 2006), strain localization in fresh gouge layers is likely to be a fundamental process controlling the dynamic strength of faults during seismic slip.

5. Conclusions

Calcite gouges deformed at seismic slip velocities show initial strengthening behavior before the onset of dynamic weakening. In fresh gouges, dynamic weakening occurs more rapidly at higher normal stresses and in thinner gouge layers. In gouges re-sheared following a hold period, dynamic weakening is much faster and mimics the behavior of solid cylinders of calcite marble. Microstructural observations show that localization to a high-strain shear band c. 100 μm wide is a critical precursor to dynamic weakening. Specifically, dynamic weakening is triggered by the formation of short slip surfaces in the shear band that we have interpreted as regions of local heating. Continued localization during dynamic weakening forms a through-going principal slip surface along which bulk frictional heating results in gouge recrystallization. If fresh gouge layers are formed dynamically at the rupture tip or due to asperity interaction during the first increments of seismic slip, a significant amount of displacement may be required to overcome the initial strengthening behavior and transition to dynamic weakening.

Acknowledgements

Elena Spagnuolo contributed the data on solid cylinders of calcite marble. Michele Fondriest, Tom Mitchell, Brooks Proctor and John Platt are thanked for constructive discussions on gouge deformation. Kat Lilly and Marco Brenna provided assistance with the SEM in the Otago Centre for Electron Microscopy (OCEM) at the University of Otago. The authors acknowledge funding from European Union Starting Grants (projects USEMS and NOFEAR to Di Toro) and a 2014 University of Otago Research Grant (to Smith).

626 **References**

627 Barnhoorn, A., Bystricky, M., Burlini, L., Kunze, K., 2004. The role of recrystallisation on the
628 deformation behaviour of calcite rocks: large strain torsion experiments on Carrara marble. Journal of
629 Structural Geology 26, 885-903.

630 Beeler, N.M., Tullis, T.E., Blanpied, M.L., Weeks, J.D., 1996. Frictional behavior of large
631 displacement experimental faults. Journal of Geophysical Research 101, 8697-8715.

632 Beeler, N.M., Tullis, T.E., Goldsby, D.L., 2008. Constitutive relationships and physical basis of fault
633 strength due to flash heating. Journal of Geophysical Research-Solid Earth 113.

634 Ben-Zion, Y., Sammis, C.G., 2003. Characterization of fault zones. Pure and Applied Geophysics 160,
635 677-715.

636 Bestmann, M., Kunze, K., Matthews, A., 2000. Evolution of a calcite marble shear zone complex on
637 Thassos Island, Greece: microstructural and textural fabrics and their kinematic significance. Journal of
638 Structural Geology 22, 1789-1807.

639 Bestmann, M., Prior, D.J., 2003. Intragranular dynamic recrystallisation in naturally deformed calcite
640 marble: diffusion accommodated grain boundary sliding as a result of subgrain rotation
641 recrystallisation. Journal of Structural Geology 25, 1597-1613.

642 Boullier, A.M., Yeh, E.-C., Boutareaud, S., Song, S.-R., Tsai, C.-H., 2009. Microscale anatomy of the
643 1999 Chi-Chi earthquake fault zone. Geochemistry Geophysics Geosystems 10, Q03016,
644 doi:03010.01029/02008GC002252.

645 Brantut, N., Han, R., Shimamoto, T., Findling, N., Schubnel, A., 2011. Fast slip with inhibited
646 temperature rise due to mineral dehydration: Evidence from experiments on gypsum. Geology 39, 59-
647 62.

648 Bruhn, R.L., Parry, W.T., Yonkee, W.A., Thompson, T., 1994. Fracturing and Hydrothermal Alteration
649 in Normal-Fault Zones. Pure and Applied Geophysics 142, 609-644.

650 Burkhard, M., 1990. Ductile deformation mechanisms in micritic limestones naturally deformed at low-
651 temperatures (150-350°C), in: Knipe, R.J., Rutter, E.H. (Eds.), Deformation Mechanisms, Rheology
652 and Tectonics. Geological Society of London, pp. 241-257.
653 Caine, J.S., Evans, J.P., Forster, C.B., 1996. Fault zone architecture and permeability structure.
654 Geology 24, 1025-1028.
655 Candela, T., Renard, F., Bouchon, M., Brouste, A., Marsan, D., Schmittbuhl, J., Voisin, C., 2009.
656 Characterization of Fault Roughness at Various Scales: Implications of Three-Dimensional High
657 Resolution Topography Measurements. Pure and Applied Geophysics 166, 1817-1851.
658 Chester, Logan, J.M., 1987. Composite planar fabric of gouge from the Punchbowl fault, California.
659 Journal of Structural Geology 9, 621-634.
660 Chester, F.M., Chester, J.S., 1998. Ultracataclasite structure and friction processes of the Punchbowl
661 fault, San Andreas system, California. Tectonophysics 295, 199-221.
662 Chester, F.M., Chester, J.S., Kirschner, D.L., Schulz, S.E., Evans, J.P., 2004. Structure of large-
663 displacement, strike-slip fault zones in the brittle continental crust, in: Karner, G.D., Taylor, B.,
664 Driscoll, N.W., Kohlstedt, D.L. (Eds.), Rheology and deformation in the lithosphere at Continental
665 Margins. Columbia University Press, New York.
666 Chiarabba, C., Amato, A., Anselmi, M., Baccheschi, P., Bianchi, I., Cattaneo, M., Cecere, G.,
667 Chiaraluce, L., Ciaccio, M.G., De Gori, P., De Luca, G., Di Bona, M., Di Stefano, R., Faenza, L.,
668 Govoni, A., Improta, L., Lucente, F.P., Marchetti, A., Margheriti, L., Mele, F., Michelini, A.,
669 Monachesi, A., Moretti, M., Pastori, M., Piana Agostinetti, N., Piccinini, D., Roselli, R., Seccia, D.,
670 Valoroso, L., 2009. The 2009 L'Aquila (central Italy) M_W6.3 earthquake: Main shock and aftershocks.
671 Geophysical Research Letters 36, L18308, doi:18310.11029/12009GL039627.
672 Chiaraluce, L., 2012. Unravelling the complexity of Apenninic extensional fault systems: A review of
673 the 2009 L'Aquila earthquake (Central Apennines, Italy). Journal of Structural Geology 42, 2-18.

674 Collettini, C., Viti, C., Tesei, T., Mollo, S., 2013. Thermal decomposition along natural carbonate
675 faults during earthquakes. Geology In Press.
676 De Paola, N., Collettini, C., Faulkner, D.R., Trippetta, F., 2008. Fault zone architecture and
677 deformation processes within evaporitic rocks in the upper crust. Tectonics 27, TC4017.
678 De Paola, N., Hirose, T., Mitchell, T., Di Toro, G., Viti, C., Shimamoto, T., 2011. Fault lubrication and
679 earthquake propagation in thermally unstable rocks. Geology 39, 35-38.
680 Di Toro, G., Goldsby, D.L., Tullis, T.E., 2004. Friction falls towards zero in quartz rock as slip velocity
681 approaches seismic rates. Nature 427, 436-439.
682 Di Toro, G., Han, R., Hirose, T., De Paola, N., Nielsen, S., Mizoguchi, K., Ferri, F., Cocco, M.,
683 Shimamoto, T., 2011. Fault lubrication during earthquakes. Nature 471, 494-498.
684 Di Toro, G., Hirose, T., Nielsen, S., Pennacchioni, G., Shimamoto, T., 2006. Natural and experimental
685 evidence of melt lubrication of faults during earthquakes. Science 311, 647-649.
686 Di Toro, G., Niemeijer, A., Tripoli, A., Nielsen, S., Di Felice, F., Scarlato, P., Spada, G., Alessandroni,
687 R., Romeo, G., Di Stefano, G., Smith, S., Spagnuolo, E., Mariano, S., 2010. From field geology to
688 earthquake simulation: a new state-of-the-art tool to investigate rock friction during the seismic cycle
689 (SHIVA). Rend Lincei-Sci Fis 21, 95-114.
690 Ebert, A., Herwegh, M., Pfiffner, A., 2007. Cooling induced strain localization in carbonate mylonites
691 within a large-scale shear zone (Glarus thrust, Switzerland). Journal of Structural Geology 29, 1164-
692 1184.
693 Engelder, J.T., 1974. Cataclasis and the generation of fault gouge. Geological Society of America
694 Bulletin 85, 1515-1522.
695 Faulkner, D.R., Jackson, C.A.L., Lunn, R.J., Schlische, R.W., Shipton, Z.K., Wibberley, C.A.J.,
696 Withjack, M.O., 2010. A review of recent developments concerning the structure, mechanics and fluid
697 flow properties of fault zones. Journal of Structural Geology 32, 1557-1575.

698 Ferri, F., Di Toro, G., Hirose, T., Han, R., Noda, H., Shimamoto, T., Quaresimin, M., de Rossi, N.,
699 2011. Low- to high-velocity frictional properties of the clay-rich gouges from the slipping zone of the
700 1963 Vaiont slide, northern Italy. Journal of Geophysical Research-Solid Earth 116.
701 Fondriest, M., Smith, S.A.F., Candela, T., Nielsen, S., Mair, K., Di Toro, G., 2013. Mirror-like faults
702 and power dissipation during earthquakes. Geology 41, 1175-1178.
703 Fondriest, M., Smith, S.A.F., Di Toro, G., Zampieri, D., Mittempergher, S., 2012. Fault zone structure
704 and seismic slip localization in dolostones, an example from the Southern Alps, Italy. Journal of
705 Structural Geology 45, 52-67.
706 Giger, S.B., Cox, S.F., Tenthorey, E., 2008. Slip localization and fault weakening as a consequence of
707 fault gouge strengthening - Insights from laboratory experiments. Earth and Planetary Science Letters
708 In Press.
709 Goldsby, D.L., Tullis, T.E., 2011. Flash Heating Leads to Low Frictional Strength of Crustal Rocks at
710 Earthquake Slip Rates. Science 334, 216-218.
711 Gratier, J.P., Gueydan, F., 2007. Deformation in the presence of fluids and mineral reactions: Effects of
712 fracturing and fluid-rock interaction on seismic cycles, in: Handy, M.R., Hirth, G., Hovius, N. (Eds.),
713 Dahlem Workshop Reports, Tectonic Faults: Agents of change on a dynamic earth. The MIT Press, pp.
714 319-356.
715 Griffith, Nielsen, S., Di Toro, G., Smith, S.A.F., 2010. Rough Faults, Distributed Weakening, and Off-
716 Fault Deformation. Journal of Geophysical Research 115, doi:10.1029/2009JB006925.
717 Han, R., Hirose, T., Shimamoto, T., 2010a. Strong velocity weakening and powder lubrication of
718 simulated carbonate faults at seismic slip rates. Journal of Geophysical Research 115, B03412,
719 doi:03410.01029/02008JB006136.
720 Han, R., Hirose, T., Shimamoto, T., 2010b. Strong velocity weakening and powder lubrication of
721 simulated carbonate faults at seismic slip rates. Journal of Geophysical Research-Solid Earth 115.

722 Han, R., Hirose, T., Shimamoto, T., Lee, Y., Ando, J., 2011. Granular nanoparticles lubricate faults
723 during seismic slip. Geology 39, 599-602.
724 Han, R., Shimamoto, T., Hirose, T., Ree, J.H., Ando, J., 2007. Ultralow friction of carbonate faults
725 caused by thermal decomposition. Science 316, 878-881.
726 Heesakkers, V., Murphy, S., Reches, Z., 2011. Earthquake Rupture at Focal Depth, Part I: Structure
727 and Rupture of the Pretorius Fault, TauTona Mine, South Africa. Pure and Applied Geophysics 168,
728 2395-2425.
729 Herwegh, M., Kunze, K., 2002. The influence of nano-scale second-phase particles on deformation of
730 fine grained calcite mylonites. Journal of Structural Geology 24, 1463-1478.
731 Ikari, M.J., Marone, C., Saffer, D.M., 2011. On the relation between fault strength and frictional
732 stability. Geology 39, 83-86.
733 Jackson, J., 1994. Active Tectonics of the Aegean Region. Annual Review of Earth and Planetary
734 Sciences, 239-271.
735 Kim, J.W., Ree, J.H., Han, R., Shimamoto, T., 2010. Experimental evidence for the simultaneous
736 formation of pseudotachylyte and mylonite in the brittle regime. Geology 38, 1143-1146.
737 Kitajima, H., Chester, J.S., Chester, F.M., Shimamoto, T., 2010. High-speed friction of disaggregated
738 ultracataclasite in rotary shear: Characterization of frictional heating, mechanical behavior, and
739 microstructure evolution. Journal of Geophysical Research-Solid Earth 115.
740 Kohli, A.H., Goldsby, D.L., Hirth, G., Tullis, T., 2011. Flash weakening of serpentinite at near-seismic
741 slip rates. Journal of Geophysical Research-Solid Earth 116.
742 Li, H., Wang, H., Xu, Z., Pei, J., Li, T., Huang, Y., Song, S.-R., Kuo, L.-W., Sun, Z., Chevalier, M.-L.,
743 Liu, D., 2012. Characteristics of the fault-related rocks, fault zones and the principal slip zone in the
744 Wenchuan Earthquake Fault Scientific Drilling Project Hole-1 (WFSD-1). Tectonophysics 584, 23-42.

745 Logan, J.M., Friedman, M., Higgs, N., Dengo, C., Shimamoto, T., 1979. Experimental studies of
746 simulated gouge and their application to studies of natural fault zones, Proceedings of Conference VIII
747 on analysis of actual fault zones in bedrock. U.S. Geological Survey Open-File Report pp. 79-1239.
748 Mair, K., Marone, C., 1999. Friction of simulated fault gouge for a wide range of velocites and normal
749 stresses. Journal of Geophysical Research 104, 28899-28914.
750 Marone, C., 1998. Laboratory-derived friction laws and their application to seismic faulting. Annual
751 Review of Earth and Planetary Sciences 26, 643-696.
752 Marone, C., Raleigh, C.B., Scholz, C.H., 1990. Frictional behaviour and constitutive modeling of
753 simulated fault gouge. Journal of Geophysical Research 95, 7007-7025.
754 Mitchell, T.M., Smith, S.A.F., Anders, M.H., Di Toro, G., Nielsen, S., Cavallo, A., Beard, A.D., 2014.
755 Catastrophic emplacement of giant landslides aided by thermal decomposition: Heart Mountain,
756 Wyoming. Earth and Planetary Science Letters In Press.
757 Mizoguchi, K., Hirose, T., Shimamoto, T., Fukuyama, E., 2008. Internal structure and permeability of
758 the Nojima fault, southwest Japan. Journal of Structural Geology 30, 513-524.
759 Nielsen, S., Di Toro, G., Hirose, T., Shimamoto, T., 2008. Frictional melt and seismic slip. Journal of
760 Geophysical Research-Solid Earth 113.
761 Niemeijer, A., Di Toro, G., Nielsen, S., Di Felice, F., 2011. Frictional melting of gabbro under extreme
762 experimental conditions of normal stress, acceleration, and sliding velocity. Journal of Geophysical
763 Research-Solid Earth 116.
764 Niemeijer, A.R., Spiers, C.J., Peach, C.J., 2008. Frictional behaviour of simulated quartz fault gouges
765 under hydrothermal conditions: Results from ultra-high strain rotary shear experiments.
766 Tectonophysics 460, 288-303.

767 Otsuki, K., Monzawa, N., Nagase, T., 2003. Fluidization and melting of fault gouge during seismic
768 slip: Identification in the Nojima fault zone and implications for focal earthquake mechanisms. Journal
769 of Geophysical Research-Solid Earth 108, 2192, doi:2110.1029/2001JB001711.
770 Power, W.L., Tullis, T.E., Brown, S.R., Boitnott, G.N., Scholz, C.H., 1987. Roughness of natural fault
771 surfaces. Geophysical Research Letters 14, 29-32.
772 Power, W.L., Tullis, T.E., Weeks, J.D., 1988. Roughness and wear during brittle faultin. Journal of
773 Geophysical Research 93, 15268-15278.
774 Proctor, B., Mitchell, T.M., Hirth, G., Goldsby, D., Zorzi, F., Di Toro, G., 2014. Dynamic weakening
775 of serpentinite gouges and bare-surfaces at seismic slip rates. Journal of Geophysical Research-Solid
776 Earth In Review.
777 Rathbun, A.P., Marone, C., 2010. Effect of strain localization on fictional behaviour of sheared
778 granular materials. Journal of Geophysical Research 115.
779 Reches, Z., Dewers, T.A., 2005. Gouge formation by dynamic pulverization during earthquake rupture.
780 Earth and Planetary Science Letters 235, 361-374.
781 Reches, Z., Lockner, D.A., 2010. Fault weakening and earthquake instability by powder lubrication.
782 Nature 467, 452-455.
783 Ree, J.H., Ando, J.I., Han, R., Shimamoto, T., 2014. Coseismic microstructures of experimental fault
784 zones in Carrara marble. Journal of Structural Geology 66, 75-83.
785 Rice, J.R., 2006. Heating and weakening of faults during earthquake slip. Journal of Geophysical
786 Research-Solid Earth 111.
787 Rodriguez-Navarro, C., Ruiz-Agudo, E., Luque, A., Rodriguez-Navarro, A.B., Ortega-Huertas, M.,
788 2009. Thermal decomposition of calcite: Mechanisms of formation and textural evolution of CaO
789 nanocrystals. American Mineralogist 94, 578-593.

790 Sagy, A., Brodsky, E., 2009. Geometric and rheological asperities in an exposed fault zone. Journal of
791 Geophysical Research 114, B02301, doi:02310.01029/02008JB005701.
792 Sagy, A., Brodsky, E.E., Axen, G.J., 2007. Evolution of fault-surface roughness with slip. Geology 35,
793 283-286.
794 Sammis, C.G., Ben-Zion, Y., 2008. Mechanics of grain-size reduction in fault zones. Journal of
795 Geophysical Research-Solid Earth 113.
796 Samtani, M., Dollimore, D., Alexander, K.S., 2002. Comparison of dolomite decomposition kinetics
797 with related carbonates and the effect of procedural variables on its kinetic parameters. Thermochim
798 Acta 392, 135-145.
799 Sawai, M., Shimamoto, T., Togo, T., 2012. Reduction in BET surface area of Nojima fault gouge with
800 seismic slip and its implication for the fracture energy of earthquakes. Journal of Structural Geology
801 38, 117-138.
802 Scholz, C.H., 1987. Wear and Gouge Formation in Brittle Faulting. Geology 15, 493-495.
803 Scholz, C.H., 2002. The Mechanics of Earthquakes and Faulting, 2 ed. Cambridge University Press,
804 Cambridge.
805 Schulz, S.E., Evans, J.P., 2000. Mesoscopic structure of the Punchbowl Fault, Southern California and
806 the geologic and geophysical structure of active strike-slip faults. Journal of Structural Geology 22,
807 913-930.
808 Scruggs, V.J., Tullis, T.E., 1998. Correlation between velocity dependence of friction and strain
809 localization in large displacement experiments on feldspar, muscovite and biotite gouge.
810 Tectonophysics 295, 15-40.
811 Scuderi, M.M., Niemeijer, A.R., Collettini, C., Marone, C., 2013. Frictional properties and slip stability
812 of active faults within carbonate-evaporite sequences: The role of dolomite and anhydrite. Earth and
813 Planetary Science Letters, http://dx.doi.org/10.1016/j.epsl.2013.1003.1024.

814 Sibson, R.H., 1977. Fault rocks and fault mechanisms. Journal of the Geological Society, London 133,
815 191-213.
816 Sibson, R.H., 1987. Earthquake Rupturing as a Mineralizing Agent in Hydrothermal Systems. Geology
817 15, 701-704.
818 Sibson, R.H., 2003. Thickness of the seismic slip zone. Bulletin of the Seismological Society of
819 America 93, 1169-1178.
820 Smith, S.A.F., Billi, A., Di Toro, G., Spiess, R., 2011. Principal Slip Zones in Limestone:
821 Microstructural Characterization and Implications for the Seismic Cycle (Tre Monti Fault, Central
822 Apennines, Italy). Pure and Applied Geophysics 168, 2365-2393.
823 Smith, S.A.F., Di Toro, G., Kim, S., Ree, J.H., Nielsen, S., Billi, A., Spiess, R., 2013. Co-seismic
824 recrystallization during shallow earthquake slip. Geology 41, 63-66.
825 Sone, H., Shimamoto, T., 2009. Frictional resistance of faults during accelerating and decelerating
826 earthquake slip. Nature Geoscience 2, 705-708.
827 Stewart, R.A., Reimold, W.U., Charlesworth, E.G., Ortlepp, W.D., 2001. The nature of a deformation
828 zone and fault rock related to a recent rockburst at Western Deep Levels Gold Mine, Witwatersrand
829 Basin, South Africa. Tectonophysics 337, 173-190.
830 Tenthorey, E., Cox, S.F., 2006. Cohesive strengthening of fault zones during the interseismic period:
831 An experimental study. Journal of Geophysical Research-Solid Earth 111, B09202,
832 doi:09210.01029/02005JB004122.
833 Tisato, N., Di Toro, G., De Rossi, N., Quaresimin, M., Candela, T., 2012. Experimental investigation
834 of flash weakening in limestone. Journal of Structural Geology.
835 Togo, T., Shimamoto, T., 2012. Energy partition for grain crushing in quartz gouge during subseismic
836 to seismic fault motion: An experimental study. Journal of Structural Geology 38, 139-155.

837 Trullenque, G., Kunze, K., Heilbronner, R., Stunitz, H., Schmid, S.M., 2006. Microfabrics of calcite
838 ultramylonites as records of coaxial and non-coaxial deformation kinematics: Examples from the
839 Rocher de l'Yret shear zone (Western Alps). Tectonophysics 424, 69-97.
840 Verberne, B.A., He, C.R., Spiers, C.J., 2010. Frictional Properties of Sedimentary Rocks and Natural
841 Fault Gouge from the Longmen Shan Fault Zone, Sichuan, China. Bulletin of the Seismological
842 Society of America 100, 2767-2790.
843 Violay, M., Nielsen, S., Spagnuolo, E., Cinti, D., Di Toro, G., Di Stefano, G., 2013. Pore fluid in
844 experimental calcite-bearing faults: Abrupt weakening and geochemical signature of co-seismic
845 processes. Earth and Planetary Science Letters 361, 74-84.
846 Wibberley, C.A.J., Shimamoto, T., 2003. Internal structure and permeability of major strike-slip fault
847 zones: the Median Tectonic Line in Mie Prefecture, Southwest Japan. Journal of Structural Geology 25,
848 59-78.
849 Yao, L., Ma, S.L., Shimamoto, T., Togo, T., 2013a. Structures and high-velocity frictional properties of
850 the Pingxi fault zone in the Longmenshan fault system, Sichuan, China, activated during the 2008
851 Wenchuan earthquake. Tectonophysics 599, 135-156.
852 Yao, L., Shimamoto, T., Ma, S.L., Han, R., Mizoguchi, K., 2013b. Rapid postseismic strength recovery
853 of Pingxi fault gouge from the Longmenshan fault system: Experiments and implications for the
854 mechanisms of high-velocity weakening of faults. Journal of Geophysical Research-Solid Earth 118,
855 4547-4563.

856

857